

Divacancy-tin complexes in electron-irradiated silicon studied by EPR

M. Fanciulli*

Institute of Physics and Astronomy, University of Aarhus, DK-8000 Aarhus C, Denmark

J. R. Byberg

Institute of Chemistry, University of Aarhus, DK-8000 Aarhus C, Denmark

(Received 22 July 1999)

n- and *p*-type float-zone silicon containing 10^{18}-cm^{-3} tin were irradiated with 2 MeV electrons to a dose of 10^{18} cm^{-2} and subsequently examined by electron paramagnetic resonance (EPR). The *p*-type material yields only the well-known Si-G29 signal due to the tin-vacancy complex SnV^0 , whereas the as-irradiated *n*-type material in addition displays the Si-G7 signal (V_2^-), DK4, recently assigned to SnV^- in a set of slightly inequivalent configurations, and a new signal DK1, from a defects with $S=1/2$ containing one tin nucleus. DK1, which we assign to $(\text{SnV-V})^-$, undergoes a reversible triclinic-monoclinic transformation at ≈ 15 K. Annealing at 428 K removes Si-G29 and DK4 and produces a six-fold increase of Si-G7 and DK1, the kinetics indicating that about 50% of SnV is transformed into V_2 and (SnV-V) . Annealing at 503 K destroys Si-G7 and DK1, the decay of DK1 being linked to the emergence of two new signals DK2 and DK3 from defects with $S=1/2$, monoclinic-*I* symmetry, and two equivalent tin nuclei each, which we identify as $(\text{SnV-VSn})^-$ and $(\text{Sn}_2\text{V-V})^-$. The structures of the tin-divacancy complexes are discussed in terms of modifications imposed on the basic divacancy structure by the larger size and lower ionization potential of the tin atom as compared to silicon. A model is proposed for the migration of (SnV-V) in the lattice at 500 K, indicated by the process $(\text{SnV-V})+\text{Sn}\rightarrow(\text{SnV-VSn})$.

I. INTRODUCTION

Point defects produced in silicon by electron irradiation have been studied for about four decades. As a result of this effort, a quite complete understanding has developed of simple intrinsic defects such as the monovacancy¹⁻⁸ and the divacancy⁹⁻¹⁵ as well as of many impurity-vacancy complexes, interstitial impurities, and other extrinsic defects. Much of the structural information has been obtained by electron paramagnetic resonance (EPR) spectroscopy and the related electron-nuclear double resonance (ENDOR) technique. Thus, EPR and ENDOR studies have led to convincing models of the monovacancy trapped by the substitutional impurities phosphorus,¹⁶ arsenic,¹⁷ antimony,¹⁷ boron,^{18,19} aluminum,²⁰ germanium,²¹ and tin,^{22,23} and by the interstitial impurities oxygen,²⁴⁻²⁶ chromium,²⁷ and iron.²⁸ The isoelectronic impurity tin, which is studied in the present work, has come to be considered one of the most efficient traps for vacancies in silicon since the early infrared absorption measurements performed by Brelot on electron-irradiated Czochralski-grown samples.^{29,30} The presence of tin was here observed to reduce the yield of the oxygen-vacancy complex VO (the A center) by a factor of 13. Moreover, annealing of the tin-doped samples at about 200°C increased the concentrations of A centers and divacancies, a result interpreted as reflecting the release of the vacancies trapped by tin. Similar results were obtained by Svensson *et al.*³¹ EPR studies by Watkins^{22,23} revealed that the tin-vacancy complex SnV has several unusual properties. Thus, the neutral charge state (SnV^0) has a spin triplet ground state and is therefore observable by EPR. Moreover, unlike other substitutional impurities, which remain near the lattice site when trapping a monovacancy,¹⁶⁻²¹ the tin atom in SnV^0 moves towards the vacancy and occupies a ‘‘bond-center’’

position between two empty lattice sites, the complex thus constituting a divacancy with a tin atom in the center. Deep level transient spectroscopy measurements by Watkins and Troxel⁵ showed that SnV has two levels associated with double- and single-donor states, respectively. A quantitative conversion at ≈ 200 K of the radiation-produced monovacancies into SnV was observed in that study, demonstrating directly the efficient trapping of vacancies by tin. So far, SnV^0 is the only tin-related defect identified in silicon.

The observed efficient formation of impurity-vacancy complexes like SnV is linked to the mobility of the monovacancy, which, as pointed out by Brower 30 years ago,³² also suggests that impurity-multivacancy defects XV_n may arise by successive trapping of vacancies at the same impurity *X*. This process is strongly exergonic owing to the large binding energy of multivacancies (≈ 1.6 eV for the divacancy¹⁰) and may be expected to occur with a substantial probability during or after irradiations with neutrons or ions, because the high local concentrations of vacancies produced invariably lead to coagulation into multivacancy structures. Accordingly, Brower could assign three oxygen-dependent EPR signals (Si-*P*2, -*P*4, and -*P*5), observed in crucible-grown silicon after neutron irradiation, to di- and tri-vacancies associated with oxygen.³² Somewhat surprisingly, however, no further impurity-multivacancy defects in silicon were reported until the recent identification³³ of HV_2^0 and HV_3^0 in proton-implanted float-zone material. In these defects, the hydrogen atom is strongly bound to one of the silicon atoms bordering the multivacancy, thus forming a Si-H unit, which is isoelectronic with the phosphorus atom. This observation, combined with the striking similarity of the *g* tensors of HV_2^0 and HV_3^0 with those of the B2 and H10 centers observed earlier in nitrogen- and phosphorus-implanted silicon³⁴ and in neutron-irradiated, phosphorus-rich silicon,³⁵ respectively,

led to the proposal that B2 and H10 could both belong to a family of homologs of the E center (PV^0) consisting of planar multivacancies with a group-V atom as neighbor in the plane. Hence, the formation of impurity-multivacancy complexes could simply have been overlooked so far.

In contrast to irradiation with heavy particles, electron irradiation of silicon creates only a modest density of vacancies that survive the initial recombination with interstitials, implying that subsequent coagulation hardly produces multivacancies beyond the divacancy. Moreover, since the presence of vacancy traps like tin suppresses the formation of divacancies, we may assume that although the impurity-vacancy complex XV may well be a deeper vacancy-trap than X itself, the successive trapping of two vacancies at the same impurity is an unlikely event until a substantial fraction of the amount of X has already trapped one vacancy (In fact the only hint of a formation of an impurity-divacancy complex by electron irradiation stems from an n -type silicon sample, in which all the phosphorus donors had been transformed into E centers, see footnote 27 of Ref. 16). Hence, as long as the impurities X outnumber the vacancies produced, the irradiation builds up a store of trapped monovacancies, which eventually participate in the making of new defects when they become mobile in the lattice at some temperature typically within the range 400–500 K. The impurity-vacancy complexes may either remain bound at this stage and migrate by alternating dissociations and recombinations, as proposed for the E centers,¹⁷ or they may dissociate completely, yielding “free” monovacancies, as assumed for SnV to account for the thermal formation of A centers and divacancies.^{29–31} Even in the latter case, however, the monovacancies are unbound for only a small fraction of the time: Owing to the low barrier for migration of the monovacancy (≈ 0.3 eV, Ref. 1) compared to the binding energy of the impurity-vacancy complex (≥ 1 eV), the escaping vacancies virtually jump from one impurity atom to another. Accordingly, most of the vacancy-vacancy encounters implied by the production of divacancies probably occur at the impurities when vacancies happen to jump to impurity atoms that are already occupied. This immediately suggests that impurity-divacancy complexes may also arise from such encounters. In the present EPR study of electron-irradiated float-zone silicon containing tin a thermal formation of the tin-divacancy complex SnV_2 is observed to occur in parallel with the formation of isolated divacancies when the tin-monovacancy complex SnV decays at ≈ 430 K, indicating that a vacancy liberated from one SnV can indeed become trapped at another. Like SnV , SnV_2 has unusual properties: The negative charge state observed by EPR exhibits a change of effective symmetry from triclinic to monoclinic- I , associated with a rapid motion of the tin atom, at a temperature as low as 15 K and, moreover, the whole defect becomes mobile in the lattice at 500 K, which eventually leads to formation of the di-tin-divacancy structures $SnV-VSn$ and Sn_2V-V , also observed by EPR in their negative charge states.

The remainder of the paper is organized as follows: Sec. II contains the experimental details; in Sec. III, we describe the new EPR signals from tin-related defects and interpret the structural information conveyed by the observed spin Hamiltonian parameters within the framework of the well-established models of the divacancy and of SnV^0 , while the

thermal and light-induced transformations of the defects are discussed in Sec. IV, and Sec. V summarizes our main results.

II. EXPERIMENTAL DETAILS

The investigated samples were float-zone silicon containing tin enriched to $\approx 85\%$ ^{119}Sn . The concentration was determined by secondary ion mass spectroscopy to be $[Sn] = 1 \times 10^{18} \text{ cm}^{-3}$. The n -type material was doped with $5 \times 10^{16} \text{ cm}^{-3}$ P, and the p -type material with $1 \times 10^{16} \text{ cm}^{-3}$ B. From the intensity of the infrared absorption line at 607 cm^{-1} ascribed to substitutional carbon, the carbon concentration was estimated to be $3 \times 10^{17} \text{ cm}^{-3}$. Discs of thickness 2 mm cut parallel to (001) were irradiated at room temperature with 2 MeV electrons to a dose of $1 \times 10^{18} \text{ e cm}^{-2}$. From these discs EPR samples measuring approximately $8 \times 4 \times 2 \text{ mm}^3$ were cut with faces parallel to (110) and (010) and subsequently etched with HNO_3 and HF to remove paramagnetic surface defects.

EPR spectra were recorded with a Bruker ESP300E spectrometer operated at X band (9.3 GHz) in the absorption mode. The static magnetic field was modulated at 100 kHz or 1.2 kHz, except when resolution enhancement via third-harmonic detection was employed.^{33,36,37} In that case, the field modulation frequency was set to 33 kHz while the EPR signal was detected at 100 kHz. The microwave frequency ν_0 and the magnetic field \mathbf{B}_0 were monitored continuously with an electronic counter and an NMR gaussmeter.

Sample temperatures in the range 5–300 K were obtained with an APC Heli-Tran liquid-helium flow cryostat. The samples were attached with epoxy resin to a silver rod (3.5 mm in diameter, 60 mm long) that was screwed into the cold block of the cryostat and thermally shielded by a thin-walled, silvered brass tube (6 mm in diameter). A quartz tube (10 mm in diameter) serving as a vacuum shroud allowed the samples to be centered in the room-temperature cavity. The samples were mounted on the $(1\bar{1}0)$ face, i.e., with $[1\bar{1}0]$ along the axis of the cryostat-cavity assembly. The magnet could be rotated about this axis, thus causing \mathbf{B}_0 to scan the $(1\bar{1}0)$ plane. By means of the extreme anisotropy of the SnV^0 signal, \mathbf{B}_0 could be aligned with any of the three main axes [001], [110], and [111], lying in this plane, to within $0^\circ.05$. The temperature of the cold block was monitored and controlled by a calibrated $\text{Al}_x\text{Ga}_{1-x}\text{As}$ diode in conjunction with a Lake Shore 330 temperature controller. No difference between the temperature of the sample and that of the cold block was found by earlier measurements in the range 2.8–30 K with this setup.³⁸ However, because fairly large samples are used here, the exposure to thermal radiation from surfaces at room temperature may create temperature gradients leading to a mean sample temperature a few degrees above the block temperature. Sample temperatures from 100 to 570 K were obtained with a Varian variable temperature device employing a N_2 gas flow, as described in Ref. 33.

The spin Hamiltonian parameters representing the EPR signals discussed here were derived from the line positions measured for \mathbf{B}_0 aligned with the three main axes. The g tensors and the hyperfine tensors associated with ^{119}Sn were obtained by an iterative numerical procedure based on first-

order perturbation theory. The final set of spin Hamiltonian parameters was in each case checked against an angular scan in the $(1\bar{1}0)$ plane, recorded at 5° intervals. The hyperfine tensors describing the positions of satellite lines arising from ^{29}Si nuclei were taken from the outset to be axial with the unique axis along a $\langle 111 \rangle$ axis, so that only two parameters per tensor, rather than six, had to be determined. This turned out to be an adequate approximation. We determined the remaining parameters (A_Z , $A_X=A_Y$) by trial and error, calculating in each step the entire EPR signal for \mathbf{B}_0 along the three main axes.

An estimate of the concentration of SnV^0 was obtained by means of a Si:P reference. From an n -type float-zone Si wafer ($300\ \mu\text{m}$ thick) with a phosphorus concentration of $5.7 \times 10^{15}\ \text{cm}^{-3}$, determined by capacitance-voltage (C-V) measurements, a slab was cut to match the large face of the sample and glued with epoxy resin onto the sample. The resin was cured at 100°C for one hour to ensure a very good thermal contact between sample and reference. The EPR signals of SnV^0 and P^0 were measured for $\mathbf{B}_0 \parallel [110]$ at 20 K. A low-microwave power level ($0.63\ \mu\text{W}$) was employed to avoid saturation effects. The relative intensities of the signals were determined by numerical double integration. Taking into account the different masses of sample and reference, and the very different transition matrix elements of the SnV^0 and P^0 signals, and correcting for the fact that the EPR transition of SnV^0 observed at X band for $\mathbf{B}_0 \parallel [110]$ connects the two upper levels of the triplet state, we obtain a measure of the concentration of SnV^0 in the sample based on the C-V measurement on the reference.

Annealings in the temperature range 300–570 K were carried out *in situ* in a N_2 flow, whereas annealings at higher temperatures (which destroyed the epoxy resin), were made *ex situ* in an Ar flow.

III. RESULTS AND DISCUSSION

A. EPR signals

1. As-irradiated samples (n -type)

As expected from the previous studies cited above, the Si-G29 signal (SnV^0) dominates the EPR spectrum of the as-irradiated n -type samples. This signal, recorded at 15 K for $\mathbf{B}_0 \parallel \langle 100 \rangle$, is shown in Fig. 1(a). At this orientation of \mathbf{B}_0 , only one group of lines is observed, corresponding to the electronic transition $M_s: 0 \leftrightarrow +1$ in the high-field limit (cfr. Fig. 4 of Ref. 22). The pair of strong outer lines arise from hyperfine interaction with ^{119}Sn nuclei ($I=1/2$), whereas the central line represents those defects containing an even isotope of tin ($I=0$). The pairs of satellite lines located symmetrically with respect to the main lines stem from hyperfine interaction with ^{29}Si nuclei ($I=1/2$, abundance 4.7%) occupying six equivalent silicon sites. The intensity of the outer lines relative to that of the central line is an accurate measure of the isotopic composition of Sn. The simulated signal, shown in Fig. 1(b), was calculated from the reported spin Hamiltonian parameters pertinent to $^{119}\text{SnV}^0$ (Ref. 22) with the admixture of the signal corresponding to 13% even tin isotopes. From the close fit to the experimental curve we conclude that the abundance of ^{119}Sn is 87%. The absence of lines at the spectral positions predicted for $^{117}\text{SnV}^0$ by

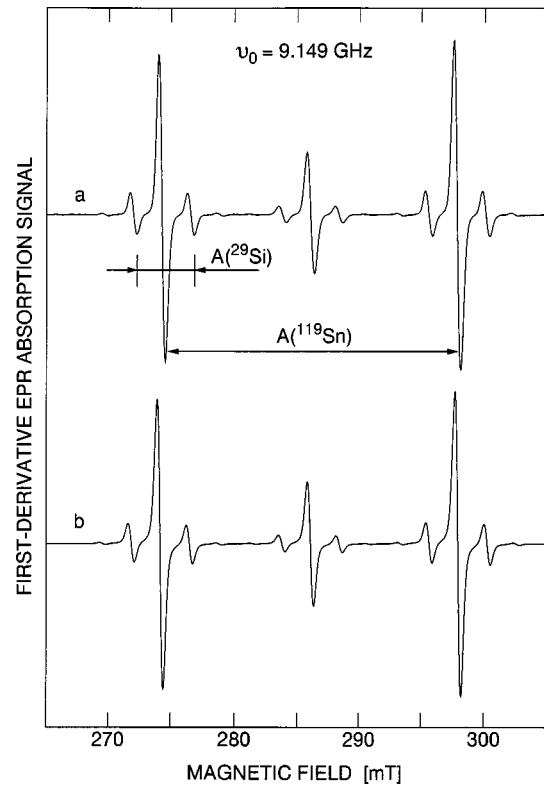


FIG. 1. EPR signal Si-G29 (SnV^0) obtained from an as-irradiated n -type sample at 15 K with $\mathbf{B}_0 \parallel \langle 001 \rangle$ (curve a). The microwave power was 3.2 mW. Hyperfine splittings arising from ^{119}Sn and ^{29}Si , which both have nuclear spin $I=1/2$, are indicated. Curve (b) is a simulation calculated from the spin Hamiltonian parameters reported in Ref. 22 (see Table I) and the assumed isotopic composition of tin: 87% ^{119}Sn and 13% even isotopes ($I=0$). The peak-to-peak linewidth is 0.5 mT.

means of the ratio of the nuclear moments indicates a negligible abundance of ^{117}Sn , which is the only other stable isotope of tin with nonzero spin. By comparison with the Si:P reference, the concentration of SnV^0 was found to be $3(1) \times 10^{16}\ \text{cm}^{-3}$, leading to an introduction rate of $0.03\ \text{cm}^{-1}$ for this defect.

Owing to the large D -tensor of SnV^0 , the G29 signal is, for most orientations of \mathbf{B}_0 , located outside the spectral region characteristic of defects with $S=1/2$ and g values near 2. Here a strong, apparently isotropic line appears at $g=2.0030(1)$. The line, which is observable at room temperature, has two pairs of fairly intense satellites. The g value and the satellite splittings coincide with those reported for an unidentified cubic defect labeled generalized gradient approximation (GGA)-2.³⁹ The recent observation that the signal contains hyperfine satellites ascribable to ^{13}C nuclei in two equivalent, trigonal sites, and that the g tensor has a tiny trigonal component, enabled us to identify GGA-2 with the negative charge state of a pair of substitutional carbon atoms in nearest-neighbor position, denoted $(\text{C}_s)_2^-$, in agreement also with the results of *ab initio* calculations on a set of plausible models.⁴⁰

Cooling the sample in the absence of light makes the G29 signal appear at 120 K, but does not change the central part of the spectrum appreciably. However, upon illumination with a flash of light at any temperature below 170 K, a strong

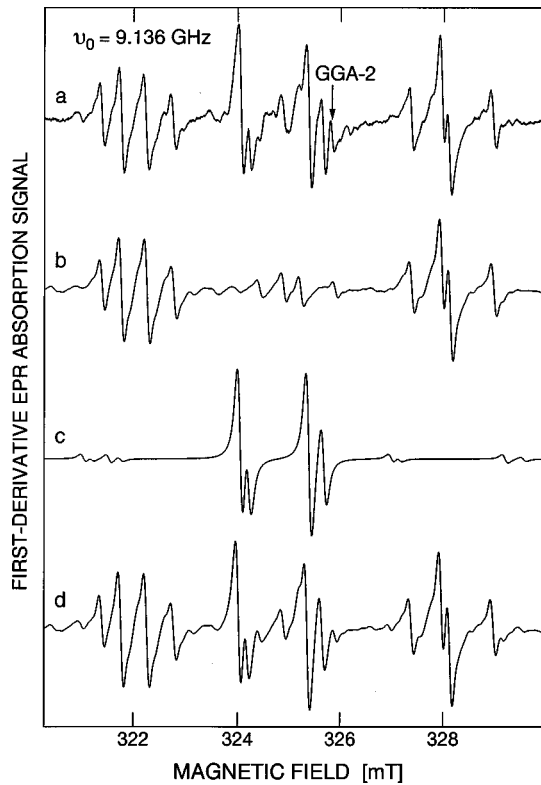


FIG. 2. Curve (a): EPR spectrum of an as-irradiated *n*-type sample, recorded with $\mathbf{B}_0 \parallel \langle 110 \rangle$ at 40 K after illumination with band-gap light. The microwave power was $2.0 \mu\text{W}$. The signals DK1 and Si-G7 dominate the spectrum. The position of the GGA-2 signal is indicated. Curves (b) and (c): simulations of DK1 (SnV_2^-) and Si-G7 (V_2^-) calculated from the spin Hamiltonian parameters (Table I) with a Lorentzian line shape of peak-to-peak width 0.14 mT. Curve (d): sum of DK1 and G7 verifying the decomposition of the experimental spectrum into these components.

signal, which we label DK1, emerges along with the Si-G7 signal arising from the negative charge state of the divacancy (V_2^-).¹⁰ Moreover, the intensity of a group of closely related weak signals, collectively denoted DK4 and assigned to SnV^- (Ref. 41), increases by a factor of about six. The flash of light simultaneously reduces G29 and GGA-2 by 40% and 90%, respectively. The simultaneous growth of DK4 and decay of G29 have been shown⁴¹ to reflect a simple transformation of SnV^0 into SnV^- . The light-induced spectral changes are all reversible: warming to room temperature restores the initial state of the sample so that only G29, GGA-2, and weak DK4 signals are detected upon subsequent cooling in the dark.

The EPR spectrum recorded at 40 K with $\mathbf{B}_0 \parallel \langle 110 \rangle$ is shown in Fig. 2(a). For this orientation of \mathbf{B}_0 , the DK1 signal consists of two groups of four strong lines each, separated by about 6.5 mT, and a corresponding weaker group of four lines at the center, partially obscured by the strong lines belonging to V_2^- . Comparison with the intensity pattern of lines associated with ^{119}Sn and the even tin isotopes (Fig. 1) immediately suggests that the separation of the groups of strong lines reflects the hyperfine interaction with a single ^{119}Sn nucleus. Moreover, each group of four lines displays the intensity ratio 1:2:2:1, indicating that two lines are doubly site degenerate for this particular orientation of \mathbf{B}_0 ,

which suggests that the splitting within the groups could arise from a *g* tensor with monoclinic-*I* symmetry. Both suggestions were confirmed by a full angular scan of the spectral positions in the (110) plane. The spin Hamiltonian parameters derived for DK1 are listed in Table I, and a simulation of the signal based on these parameters is shown as curve (b) in Fig. 2, whereas curve (c) depicts the Si-G7 signal (V_2^-), as simulated from the reported parameters,¹⁰ and curve (d) is the calculated full spectrum. At the employed microwave power, the residual GGA-2 signal is strongly suppressed by saturation and has therefore been left out. When the temperature of the sample is further decreased, the site-degenerate lines of the DK1 signal for $\mathbf{B}_0 \parallel \langle 110 \rangle$ first broaden (at ≈ 15 K) and then each split into two components at ≈ 10 K. This process, which is illustrated in Fig. 3, reflects a transition from monoclinic-*I* symmetry at 40 K to triclinic symmetry at 8 K. The spin-Hamiltonian parameters representing the triclinic signal at 8 K are included in Table I, and the corresponding simulation is shown as curve (d) in Fig. 3. We note that the signs of the principal values of the hyperfine tensor \mathbf{A}^{Sn} could not be determined. However, the relationship between the monoclinic and triclinic spin Hamiltonian discussed below allows the conclusions that all principal values have the same sign. Apart from the temperature-induced change of symmetry seen below 20 K, a peculiar temperature dependence of the ^{119}Sn hyperfine tensor is observed in the temperature range 15–120 K: as shown in Fig. 4, the absolute values of the principal hyperfine components quite unexpectedly *increase* strongly with increasing temperature, attaining a maximum value at about 70 K, and then decrease rather sharply. In contrast, the principal *g* values are constant within the limits of error up to 70 K and then decrease slightly with increasing temperature, the average reduction at 120 K being $\Delta_g = 0.0005$. The curves of Fig. 4 have a shape resembling that of the temperature dependence reported by Watkins²³ for the fine structure parameters \mathbf{D} of SnV^0 (see Fig. 3 of Ref. 23). However, since the ^{119}Sn hyperfine splitting of SnV^0 exhibits no anomalous temperature dependence similar to that of SnV_2^- , the underlying mechanisms coupling the electron spin to the atomic motion are probably different in the two cases.

Pairs of weak satellite lines ascribable to hyperfine interaction with ^{29}Si nuclei are observed in the DK1 signal both for the triclinic and the monoclinic configuration, as apparent from the curves (a) of Figs. 5 and 6, which show the signals recorded with $\mathbf{B}_0 \parallel \langle 100 \rangle$ at 8 and 70 K, respectively. At 8 K the signal displays four pairs of satellites, which are indicated at the left-hand side of curve (a), Fig. 5. The satellites correspond to ^{29}Si nuclei at four inequivalent sites. If this signal is recorded with resolution enhancement, two additional pairs of satellites emerge close to the main lines. However, the corresponding lines were poorly resolved for $\mathbf{B}_0 \parallel \langle 110 \rangle$, so that the anisotropy of the splittings could not be determined. At 70 K, four pairs of satellites are also present, but they overlap for $\mathbf{B}_0 \parallel \langle 100 \rangle$. Resolution enhancement did not bring out additional satellites at this temperature. The satellites represent ^{29}Si nuclei occupying three distinct pairs of equivalent sites related through reflection in the mirror plane of the defect (which is now monoclinic) and one single site. The observed position of the satellite lines may be represented by the inclusion of a set of axial hyperfine tensors

TABLE I. Spin Hamiltonian parameters of divacancy-tin complexes discussed in the present work. For comparison, those for V_2^- and for SnV^0 are also included. The principal values of the hyperfine interaction tensors, given in MHz, refer to ^{119}Sn and ^{29}Si nuclei. Limits of error given for \mathbf{g} and \mathbf{A}^{Sn} are the standard deviations characterizing a least-square fit to the observed line positions. Those given for \mathbf{A}^{Si} are estimates.

Term		DK1 SnV $_2^-$ (8 K)	DK1 SnV $_2^-$ (70 K)	DK2 Sn $_2$ V $_2^-$ <i>a</i> (100 K)	DK3 Sn $_2$ V $_2^-$ <i>b</i> (35 K)	Si-G7 ^a V $_2^-$ (20 K)	Si-G29 ^b SnV 0 (20 K)
	<i>S</i>	1/2	1/2	1/2	1/2	1/2	1
\mathbf{g}	g_x	2.00998(8)	2.00290(4)	2.00095(8)	2.0076(2)	2.0135	2.0025
	g_y	2.01258(8)	2.01255(4)	2.01404(6)	2.0063(2)	2.0150	2.0025
	g_z	2.00113(8)	2.00812(4)	2.00744(5)	2.0002(2)	2.0012	2.0107
	ϕ, θ, ψ^c	82.6, 65.9, 105.4	0, 19.8, 0	0, -42.4, 0	0, -76, 0	0, -61, 0	0, -54.74, 0
\mathbf{A}^{Sn}	$ A_x $	174.7(5)	178.7(3)	244.4(5) ^d	132(1) ^e		393
	$ A_y $	160.1(5)	180.2(3)	246.9(4)	87(1)		393
	$ A_z $	149.2(5)	166.3(2)	230.9(3)	100(1)		374
	ϕ, θ, ψ^c	77.2, 39.1, 74.0	0, 44.2, 0	0, -38.6, 0	-41, 20, 48		0, -54.74, 0
\mathbf{A}_1^{Si}	$A_x=A_y$	-205(2)	-99(2)	-81(1)		-171.9	-68
	A_z	-289(2) ^f	-138(2) ^g	-112(1) ^h		-241.8 ⁱ	-99 ^j
\mathbf{A}_2^{Si}	$A_x=A_y$	-100(3)	-71(2)	-27(1)		-29.2	
	A_z	-132(3) ^k	-103(2) ^g	-45(1) ^h		35.9 ^h	
\mathbf{A}_3^{Si}	$A_x=A_y$	-38(5)	-71(3)	-18(1)		16.8	
	A_z	-67(5) ^f	-85(3) ^l	-22(1) ^h		26.3 ^h	
\mathbf{A}_4^{Si}	$A_x=A_y$	-73(3)	-22(3)				
	A_z	-98(3) ^l	-37(3) ^g				

^aData from Ref. 14.

^bData from Ref. 22.

^cEulerian angles ϕ, θ, ψ (in degrees), defined in Ref. 42, specify the principal axes (*XYZ*) for one of the 24 orientations of the defect with respect to a reference coordinate system with axes $[1\bar{1}0]$, $[110]$, and $[001]$. With this choice of reference system θ is the rotation angle from $[001]$ to *Z*. For terms with (110) mirror symmetry *X* coincides with $[1\bar{1}0]$, and $\phi = \psi = 0$, $[111]$ has $\theta = -54.74$. Equation (4.47) of Ref. 42 gives the coordinates of *X*, *Y*, and *Z* in the reference coordinate system as functions of the Eulerian angles (ϕ, θ, ψ) .

^d $\mathbf{A}_1^{\text{Sn}} = \mathbf{A}_2^{\text{Sn}}$.

^e \mathbf{A}_2^{Si} is the mirror image of \mathbf{A}_1^{Sn} , having $\phi, \theta, \psi = 41, 20, -48$.

^fOne silicon site, *Z* \parallel $[\bar{1}11]$.

^gTwo equivalent silicon sites, one with *Z* \parallel $[\bar{1}11]$ and the other with *Z* \parallel $[1\bar{1}1]$.

^hFour equivalent silicon sites, two with *Z* \parallel $[\bar{1}11]$ and two with *Z* \parallel $[1\bar{1}1]$.

ⁱTwo equivalent silicon sites, *Z* nearly parallel to $[111]$.

^jSix equivalent silicon sites.

^kOne silicon site, *Z* \parallel $[1\bar{1}1]$.

^lOne silicon site, *Z* \parallel $[111]$.

\mathbf{A}_i^{Si} in the spin Hamiltonian, each with the unique axes parallel to one $\langle 111 \rangle$ axis. This suggests that the electron spin distribution can be expressed in terms of sp^3 -like combinations of atomic orbitals on the silicon atoms, in which case all principal values of each \mathbf{A}_i^{Si} have the same sign. The principal values are listed in Table I with negative sign because the nuclear *g* factor of ^{29}Si is negative, and positive-spin populations on the silicon atoms are anticipated. The

agreement obtained between calculated and observed splittings may be judged from the simulations included as the curves (b) in Figs. 5 and 6.

2. EPR signals produced by annealing

Annealing of the irradiated samples at 500 K removes the G29, G7, DK1, and DK4 signals, and generates two signals, which we label DK2 and DK3. Both are observed at low

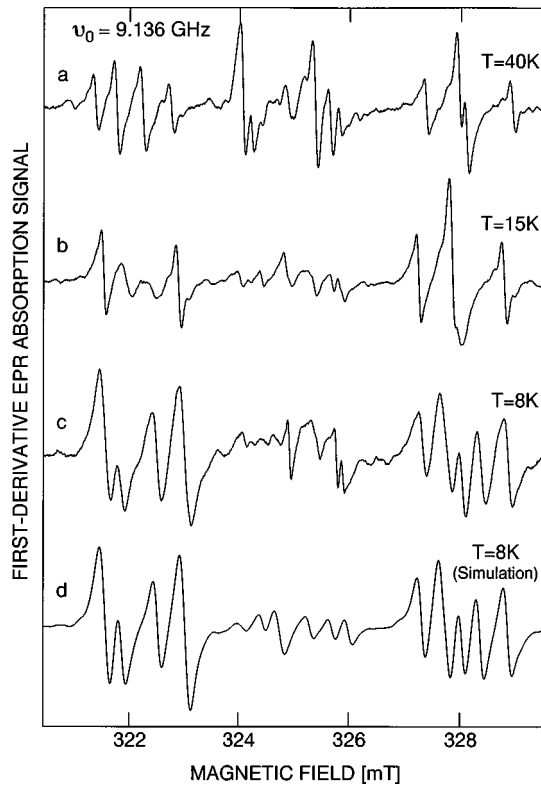


FIG. 3. Temperature dependence of the EPR spectrum shown as Fig. 2, curve (a), indicating that DK1 (SnV_2^-) undergoes a transition from monoclinic- I symmetry at 40 K to triclinic symmetry at 8 K. The most intense lines at 40 K [curve (a)] broaden at 15 K [curve (b)] and split at 8 K [curve (c)]. Curve d is calculated from the triclinic spin Hamiltonian parameters determined at 8 K (Table I) and a Lorentzian line shape of width 0.17 mT.

sample temperatures only. DK2 is well resolved and has a nearly temperature-independent linewidth below 120 K. In contrast, the linewidth of DK3 is large at 100 K, but decreases markedly down to about 40 K. This difference allows DK2 to be observed at 100 K without significant interference from DK3. Moreover, the intensities of the two signals respond differently to illumination of the sample at low temperature: a flash of light increases DK2 by a factor of ≈ 3 , whereas DK3 is unaffected by the light. Accordingly, neat representations of either DK2 or DK3 are obtainable by subtraction of spectra obtained before and after illumination of the sample. The signals obtained for $\mathbf{B}_0 \parallel \langle 100 \rangle$ are shown as curves (a) in Figs. 7 and 8. Both signals represent defects with $S=1/2$. The signals comprise five groups of intense hyperfine lines displaying the relative positions and the intensity pattern expected for defects containing two tin nuclei at equivalent positions, taking into account the actual isotopic composition. For DK2 each of the four outer groups is a pair of lines with the intensity ratio 1:2, which indicates that the g tensor as well as the tensors \mathbf{A}_i^{Sn} ($i=1,2$) describing the hyperfine interaction within the ^{119}Sn nuclei at least have monoclinic- I symmetry. An angular scan in the (110) plane showed that the symmetry of the tensors is indeed monoclinic- I . Moreover, \mathbf{A}_1^{Sn} and \mathbf{A}_2^{Sn} are equivalent for *all* orientations of \mathbf{B}_0 , implying that the sites occupied by the tin atoms are connected by inversion symmetry, from which we in turn deduce that the point group of the defect associated

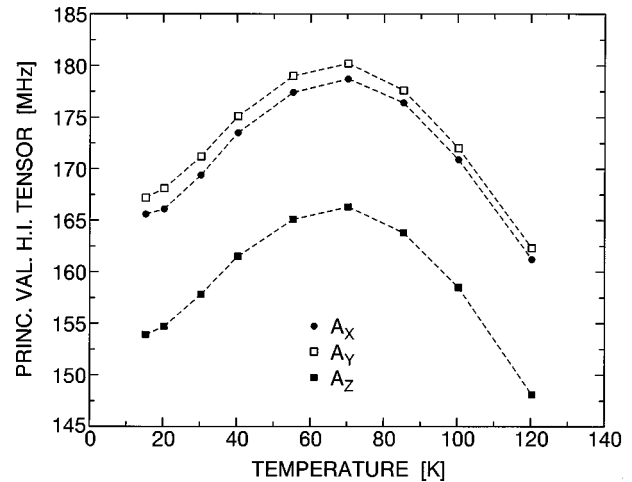


FIG. 4. Temperature dependence of the ^{119}Sn hyperfine parameters of DK1 (SnV_2^-) above the triclinic-monoclinic- I transition temperature.

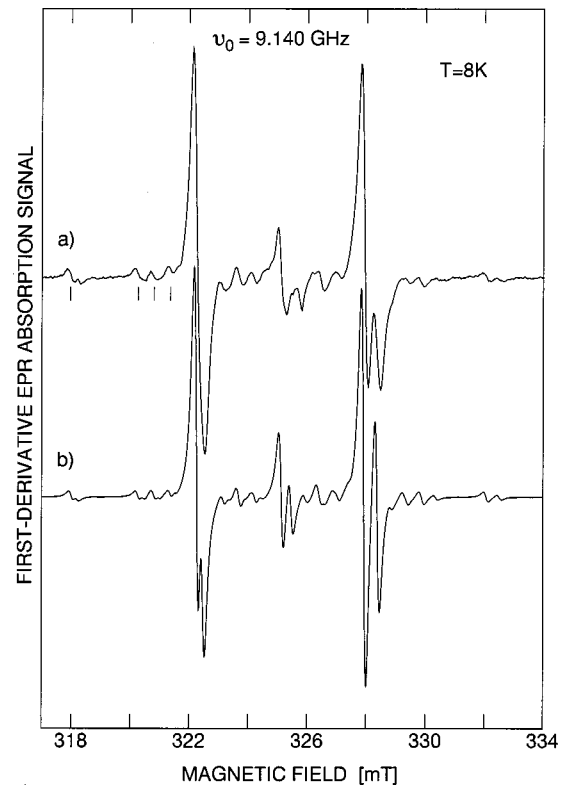


FIG. 5. Curve (a): EPR signal DK1 (SnV_2^-) recorded at 8 K with $\mathbf{B}_0 \parallel \langle 001 \rangle$ showing the ^{29}Si splittings of the triclinic configuration of SnV_2^- . The signal was recorded after illumination with band-gap light, and the spectrum obtained before the illumination was subtracted to eliminate spurious lines from weak signals that are insensitive to light. At left, satellite lines arising from ^{29}Si nuclei in four inequivalent sites are indicated. Curve (b): simulation calculated from the spin Hamiltonian parameters (Table I) and a Lorentzian line shape of width 0.17 mT, chosen to fit the shape of the satellite lines. At the employed microwave power level (20 μW), the signals G7 (V_2^-) and GGA-2 are virtually absent at 8 K because of saturation. The main ^{119}Sn hyperfine lines of DK1 and, in particular, the central pair of lines display some saturation broadening.

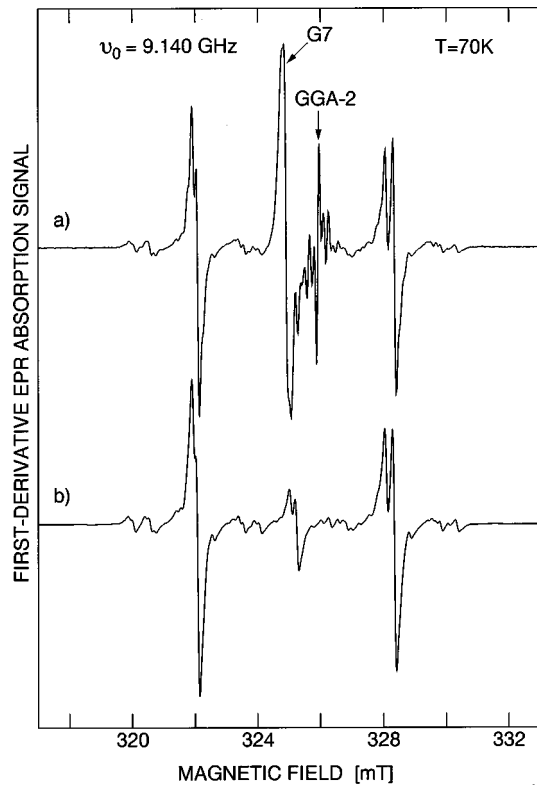


FIG. 6. Curve (a): EPR signal DK1 (SnV_2^-) recorded at 70 K with $\mathbf{B}_0 \parallel \langle 001 \rangle$, showing the ^{29}Si splittings of the monoclinic- I configuration of SnV_2^- . The signal was recorded after illumination with band-gap light and the spectrum obtained before the illumination was subtracted. As a consequence, the GGA-2 signal, which is suppressed by the illumination, appears with a phase opposite to that of DK1 and G7. Curve (b): simulation calculated from the spin Hamiltonian parameters (Table I) and a Lorentzian line shape of width 0.14 mT.

with the DK2 signal is C_{2h} . This symmetry is retained right down to 5 K. No anomalous temperature dependence of the ^{119}Sn hyperfine splitting is observed for DK2.

The less well-resolved signal DK3 [Fig. 8, curve (a)] displays a pattern closely resembling that of DK2 (apart from the accidental collapse of the left-hand pair of lines) with one important exception: the fourth group of lines from the left (marked by an arrow in the figure), which arises from defects containing only one ^{119}Sn nucleus, consists of three rather than two lines. This indicates that although the overall symmetry of the spin Hamiltonian is monoclinic- I , the individual hyperfine tensors \mathbf{A}_1^{Sn} and \mathbf{A}_2^{Sn} do not conform to this symmetry. Hence the monoclinic spectral pattern (two lines for $\mathbf{B}_0 \parallel [100]$) is observed only for defects in which the two tin nuclei are either both ^{119}Sn or both even isotopes. The point group of the defect is C_{1h} .

The DK2 signal contains well resolved satellite lines ascribable to hyperfine interaction with ^{29}Si nuclei occupying three sets of four equivalent silicon sites each. The unique axes of the corresponding hyperfine tensors are directed along the two $\langle 111 \rangle$ axes that are inclined to the mirror plane of the defect. The DK3 signal similarly exhibits satellite lines representing ^{29}Si nuclei. However, overlapping lines from an unidentified signal with the same intensity as the satellites precluded a reliable analysis of the ^{29}Si hyperfine

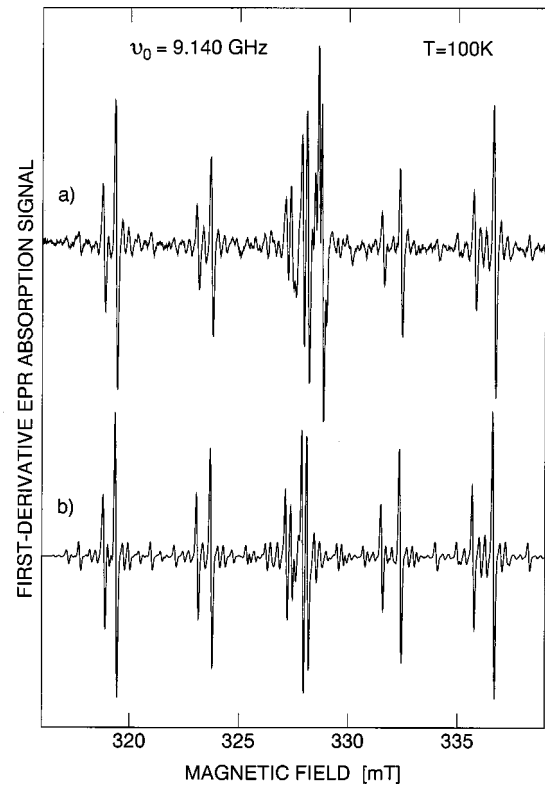


FIG. 7. Curve (a): EPR signal DK2 ($\text{Sn}_2\text{V}_2^- a$) recorded after illumination at 100 K with $\mathbf{B}_0 \parallel \langle 001 \rangle$, 6.32 mW microwave power, and with resolution enhancement by the means of third-harmonic detection. The central group of strong lines contains additional signals. Curve (b): simulation calculated from the spin Hamiltonian parameters for DK2 (Table I) and a Gaussian line shape of width 0.1 mT.

splittings for DK3. The spin Hamiltonian parameters derived for DK2 and DK3, including the ^{29}Si hyperfine parameters for DK2, are listed in Table I, and simulations of the two signals, based on these parameters, are shown as the curves (b) in Figs. 7 and 8. As for DK1 and DK4, the signs of the hyperfine parameters pertaining to ^{119}Sn could not be determined.

3. *p*-type samples

The *p*-type samples displayed a strong Si-G29 signal (SnV^0), but no other EPR signals, neither before nor after annealing to 570 K. In contrast to what was observed in *n*-type samples, a flash of light at low temperature produced no metastable changes of the EPR spectrum of these samples. The concentration of SnV^0 was found to be $8(1) \times 10^{16} \text{ cm}^{-3}$, corresponding to an introduction rate of 0.08.

B. Structure of the defects

The signals DK1, DK2, and DK3 are only observed in *n*-type material and only under conditions where also V_2^- can be observed if present. Indeed, DK1 and the V_2^- signal invariably come and go together. Moreover, the spectroscopic properties, in particular the hyperfine interactions with ^{29}Si nuclei observed in DK1 and DK2, indicate that the corresponding defects are closely related to the divacancy. Accordingly, we assign the signals DK1, DK2, and DK3, to the

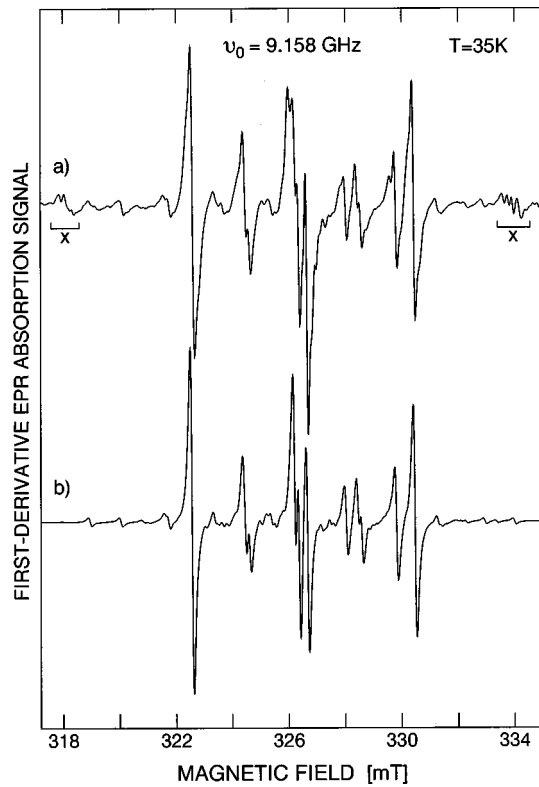


FIG. 8. Curve (a): EPR signal DK3 ($\text{Sn}_2\text{V}_2^- b$) recorded at 35 K with $\mathbf{B}_0 \parallel \langle 001 \rangle$ and 0.2 mW microwave power. Lines belonging to an unrelated signal are marked X, while the arrow indicates a group of lines which arises from defects containing only one ^{119}Sn nucleus (see Sec. III A 2). Curve (b): simulation calculated from the spin Hamiltonian parameters for DK3 (Table I) and a Gaussian line shape of width 0.13 mT. Satellite lines due to ^{29}Si nuclei in four inequivalent positions with hyperfine splittings (for $\mathbf{B}_0 \parallel \langle 001 \rangle$) 200, 112, 53, and 46 MHz, respectively, were included in the simulation.

negative charge state of three complexes, each containing a divacancy bound to one or two tin atoms, which we represent as SnV_2^- , $\text{Sn}_2\text{V}_2^- a$, and $\text{Sn}_2\text{V}_2^- b$, respectively.

Below we discuss the properties of SnV_2^- , $\text{Sn}_2\text{V}_2^- a$, and $\text{Sn}_2\text{V}_2^- b$, within the framework of the electronic structure of V_2^- ,^{9,10} thus considering the observed effects of the tin atoms as perturbations imposed on the basic divacancy structure. The proposed models of the three defects are sketched in Fig. 9. In the sketch of SnV_2^- (top) the six dangling-bond orbitals of the divacancy have been labeled (a) through (f). In the undistorted lattice geometry the axes of (a) and (f) are parallel to $[111]$, whereas the axes of (b) and (e), and those of (c) and (d), are parallel to $[1\bar{1}1]$ and $[\bar{1}11]$, respectively. The electronic structure of V_2^- , which has monoclinic- I symmetry (point group C_{2h}), may be crudely outlined in terms of “molecular orbitals” constructed from the dangling-bond orbitals:¹⁰ the two pairs of orbitals (b,c) and (d,e) form two long Si-Si bonds perpendicular to the mirror plane $(1\bar{1}0)$, whereas (a) and (f) combine across the divacancy. The bonding combination, which we may label (a+f), becomes doubly occupied, whereas the antibonding combination (a-f) holds the unpaired electron.

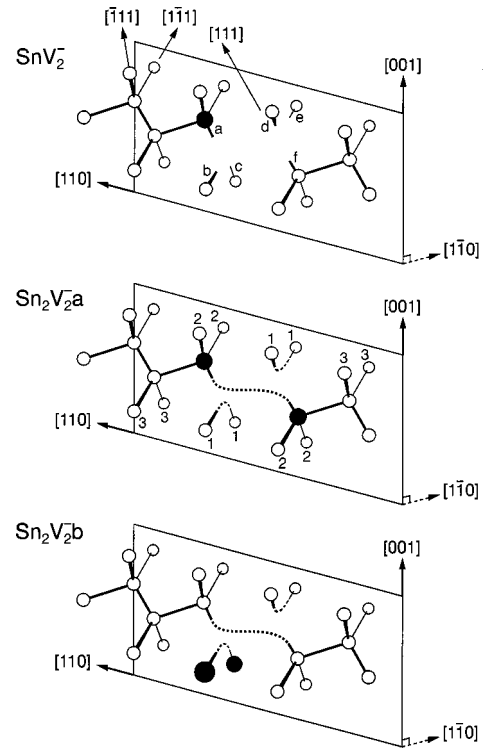


FIG. 9. Sketches of the structures proposed for the divacancy-tin complexes. Open and filled circles represent silicon and tin atoms, respectively. In the sketch of SnV_2^- (top) the dangling bonds of the divacancy are labeled by the letters a through f, and in $\text{Sn}_2\text{V}_2^- a, b$ the broken lines suggest bonds constructed from pairs of dangling bond orbitals. The ^{29}Si hyperfine splittings of the EPR signal from $\text{Sn}_2\text{V}_2^- a$ are assigned to ^{29}Si nuclei occupying the three sets of four equivalent sites labeled 1, 2, and 3 in the sketch of this defect.

1. SnV_2^-

Substituting a tin atom for one of the six equivalent silicon atoms bordering the divacancy might be expected to yield a defect belonging to the point group C_{1h} , as illustrated in Fig. 9 (top), where the tin atom is placed in the $(1\bar{1}0)$ plane. However, since the spin Hamiltonian assigned to SnV_2^- has no symmetry below 15 K, the tin atom may in fact be located *outside* the $(1\bar{1}0)$ plane. Because the covalent radius of tin is 0.27 Å larger than that of silicon, we may assume that the tin atom moves from the substitutional site towards the adjacent vacancy, as was observed earlier in SnV^0 (Ref. 22). However, at a position in the mirror plane corresponding to that seen in SnV^0 (i.e. near one “bond center” in a trivacancy) the tin atom would be surrounded by five silicon atoms, which may be energetically unfavorable. Indeed, the observed triclinic configuration of SnV_2^- suggests a relaxation of the defect that maximizes the electronic overlap of the four sp^3 orbitals of tin with sp^3 orbitals on four silicon neighbors, so that the orbital (a) on tin overlaps with only one of adjacent silicon orbitals (b) and (c) (see Fig. 9). This asymmetric structure of SnV_2^- is reminiscent of that proposed for the substitutional-boron-vacancy complex BV .¹⁸

The distribution of the electron spin among just four silicon atoms (Table I) is consistent with this picture: As discussed below, the orbital ψ_u of the unpaired electron has a

TABLE II. Spin Hamiltonian parameters for the monoclinic- I signal from SnV_2^- at 15 K. The principal values of the hyperfine interaction tensor, given in MHz, refer to ^{119}Sn . The experimental values are compared with those calculated from the corresponding parameters for the triclinic signal at 8 K by means of the jump model (see text). θ is defined in Table I.

	g_x	g_y	g_z	θ_g	A_x	A_y	A_z	θ_A
Exp.	2.0031	2.0125	2.0083	18.0	165.6	167.2	153.9	45.0
Calc.	2.0027	2.0126	2.0084	14.8	162.5	166.1	155.4	34.8

negligible amplitude on the tin atom. This suggests that the energy level associated with the orbital (a) lies substantially higher than the level of the silicon dangling bonds, in accordance with the fact that the first ionization potential of the tin atom is 0.82 eV lower than that of the silicon atom.⁴³ Therefore, a moderate overlap of the tin orbital (a) with the silicon orbital (b) will lower the energy of (b) with respect to the other silicon dangling bonds without admixing much (a). Hence, (b) becomes essentially doubly occupied and, accordingly, contributes little to the other molecular orbitals, including ψ_u .

The triclinic-monoclinic transition at ≈ 10 K may be used to establish a simple relationship between the spin Hamiltonians for the two configurations that allows an assignment of the observed ^{29}Si hyperfine splittings to specific atomic positions. The 24 distinct equivalent orientations of the triclinic defect SnV_2^- form 12 pairs of orientations related through reflection in the (110) planes of the silicon lattice. If SnV_2^- jumps between the members of such a pair at a frequency exceeding the spectral shifts distinguishing the two orientations, a motionally averaged EPR signal displaying monoclinic- I symmetry will result, as is in fact observed above 15 K. Within this model, the g and A^{Sn} tensors describing the monoclinic signal are the algebraic means of the corresponding pairs of tensors measured at low temperature. From Table II, it appears that this is indeed the case. Apart from the angle θ , which is sensitive to minor errors in the low-temperature parameters, a very satisfactory agreement between predicted and observed high-temperature parameters is obtained, strongly indicating that the triclinic-monoclinic transition is due to rapid jumps between two orientations, which probably involve a motion of the tin atom across the (110) plane. The comparison moreover serves to determine the relative signs of the principal hyperfine components, since the predicted tensor $A^{\text{Sn}}(15\text{ K})$ bears no resemblance to the observed tensor unless the same sign is assumed for *all* principal values of $A^{\text{Sn}}(8\text{ K})$. This choice of signs leads to a very small electron spin density on the tin atom, corresponding to a spin population of $\approx 0.01e$ in 5s and 5p orbitals.

Although the motion of tin may be no more than a minor displacement, it is accompanied by a large-scale electronic reorganization, causing the Z axis of the g tensor to rotate through 132° . We note that this motion resembles the motion of V_2^- observed at ≈ 60 K.¹⁰ At this temperature the plane of the monoclinic distortion, which contains the axis $Z(g)$, rotates in steps of 120° . However, V_2^- has three equivalent configurations while SnV_2^- has only two. Since the electron

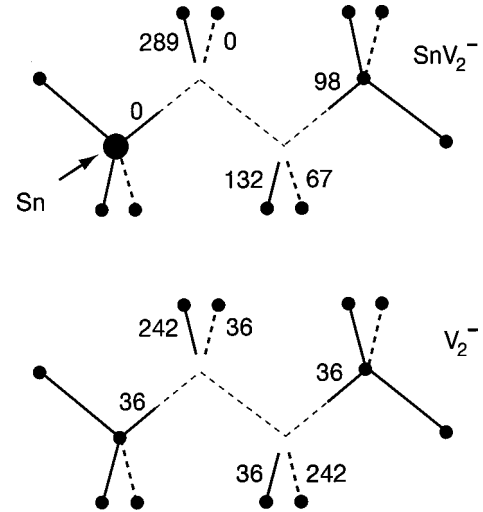


FIG. 10. Comparison of the spin populations in the dangling-bond orbitals of SnV_2^- and V_2^- . The numbers shown in the figure represent the observed value of $|A_Z^{\text{Si}}|$ (in MHz) associated with each silicon site, which is roughly proportional to the spin population. The orientation of the mirror plane of V_2^- has been chosen to bring out the similarity of the two spin distributions.

spin distribution corresponding to the monoclinic, high-temperature signal is the average of the distributions characterizing the pair of mirror-related, triclinic configurations of the defect, the ^{29}Si hyperfine tensors associated with silicon sites lying outside the mirror plane (110) come in equivalent pairs with common principal values equal to the mean of those pertaining to the same pair of silicon sites in the triclinic configuration. Accordingly, the principal values of the hyperfine tensors representing spin populations in the pairs of dangling-bond orbitals (b,c) and (d,e) should display the simple relationship $A_Z(70\text{ K}, \text{b,c}) \approx \frac{1}{2}[A_Z(8\text{ K}, \text{b}) + A_Z(8\text{ K}, \text{c})]$ and the analogous relationship for the pair (d) and (e). Assuming, as discussed above, that the orbital (b) carries no spin density, we assign $A_1(8\text{ K})$ to the orbital (c) because $A_{1Z}(70\text{ K}) \approx \frac{1}{2}A_{1Z}(8\text{ K})$. Moreover, since $A_{2Z}(70\text{ K}) \approx \frac{1}{2}[A_{2Z}(8\text{ K}) + A_{3Z}(8\text{ K})]$, $A_2(8\text{ K})$ and $A_3(8\text{ K})$ may be assigned to the orbitals (e) and (d), respectively. The hyperfine splittings represented by $A_4(8\text{ K})$ and $A_3(70\text{ K})$ probably arise from a spin population in the dangling bond orbital (f). According to the jump model, this population should be unaffected by the motion, implying $A_4(8\text{ K}) \approx A_3(70\text{ K})$. However, the unusually small anisotropy observed at 70 K suggests a reduction of the motionally averaged value of A_Z that can occur if the unique axis of $A_4(8\text{ K})$ deviates somewhat from [111]. Finally, the two smallest ^{29}Si splittings that were resolved at 8 K for $\text{B}_0 \parallel \langle 100 \rangle$ apparently correspond to the high-temperature average described by the tensor $A_3(70\text{ K})$. We thus find that the orbital ψ_u of the unpaired electron is a (presumably antibonding) combination of (c) with (d), (e), and (f). The spin distribution of SnV_2^- as mapped by the observed ^{29}Si hyperfine splittings is shown in Fig. 10 together with a similar map for V_2^- . It appears from the figure that the tin atom causes a moderate redistribution of the electron spin, mainly within the vacancy that does not contain the tin atom, so that the spin remains evenly divided between the two vacancies. In accordance with this result, the g tensor of SnV_2^- and V_2^-

have similar anisotropies apart from the magnitude of the g shifts Δg_X and Δg_Y , which are 20% smaller for SnV_2^- than for V_2^- (Table I). The unique axis $Z(g)$ deviates by only 13° from the axis of the dominant contribution (c) to ψ_u .

2. Sn_2V_2^-a

Despite the symmetry (C_{2h}) and the well-resolved ^{29}Si hyperfine splittings, some structural ambiguity remains for this defect, mainly because the position of the two tin atoms within the mirror plane are not revealed by the EPR signal. The model depicted in Fig. 9 has the tin atoms at substitutional sites at either end of the divacancy. However, a planar structure comprising a central Sn-Sn unit with a vacancy at either end is equally consistent with the observed symmetry and hyperfine splittings. Probably the tin atoms are located at positions somewhere between these extremes, allowing them to bind together as well as to form bonds with several silicon neighbors. If so, the structure may be described as a planar tetravacancy containing two tin atoms or, alternatively, as two SnV defects combined end to end.

The electron spin density of Sn_2V_2^-a is spread over sp^3 -like silicon orbitals with axes parallel to either $[1\bar{1}1]$ or $[\bar{1}11]$ on 12 atoms in three groups of four equivalent positions. The orientations of the axes indicate that these atoms all lie outside the $(1\bar{1}0)$ mirror plane of the defect. Since no spin density is found on silicon atoms in the $(1\bar{1}0)$ plane we infer that the orbital ψ_u of the unpaired electron is antisymmetric with respect to reflection in this plane, implying in turn that the tin atoms sit in a node plane of ψ_u . Assuming that the structure of Sn_2V_2^-a resembles that shown in Fig. 9 and noting that over 60% of the spin density is located on one set of four silicon atoms, which we take as those carrying the dangling-bond orbitals (b), (c), (d), and (e), we may allocate the valence electrons of the defect. As in V_2^- , the doubly occupied orbitals probably are $(b+c) \pm (d+e)$ and $(a+f)$. However, since (a) and (f) are now dangling-bond orbitals on the tin atoms and presumably form a significant Sn-Sn bond, the corresponding antibonding combination $(a-f)$ lies *above* the antibonding combination of silicon orbitals $(b-c)+(d-e)$, which therefore becomes the singly occupied orbital of Sn_2V_2^-a . This orbital, which belongs to the representation A_u , has the observed antisymmetric character and, moreover, is consistent with the concentration of a large fraction of the spin density in the four dangling bonds labeled (1) in Fig. 9. The smaller contributions reflected in the ^{29}Si hyperfine tensors \mathbf{A}_2 and \mathbf{A}_3 (see Table I) may reasonably be assigned to silicon atoms further away from the center of the defect, like those labeled (2) and (3). The g shifts of Sn_2V_2^-a resemble those of V_2^- . However, the small negative shift occurs *perpendicular* to the mirror plane rather than *in* the plane as observed for V_2^- . This observation corroborates that ψ_u for Sn_2V_2^-a belongs to the representation A_u of D_{2h} , which by symmetry has no perpendicular g shift in the usual approximation based on second-order perturbation theory.

3. Sn_2V_2^-b

While the configuration Sn_2V_2^-a arises when a tin atom is attached at either end of a divacancy and hence may be rep-

resented as $(\text{SnV-VSn})^-$, the configuration Sn_2V_2^-b results from attaching two tin atoms at the same end of V_2^- , and may be represented as $(\text{SnV}_2-\text{V})^-$, see Fig. 9. Assuming as in the previous cases that the tin atoms move from the substitutional sites towards the adjacent vacancy, we may consider the structure as a pyramidal tetravacancy containing two tin atoms near “bond-center” positions. Since the monoclinic- I symmetry of the EPR signal of Sn_2V_2^-b is retained right down to 5 K, the mirror symmetry belongs to the stable configuration itself rather than to a motionally averaged configuration like that seen in SnV_2^- . However, the line broadening observed at high temperature suggests some kind of motion of the tin atoms. Noting that a pyramidal tetravacancy has three equivalent bond-center positions, which constitute three equivalent sites for the two tin atoms of Sn_2V_2^-b , we propose that at ≈ 100 K the tin atoms jump among these three sites at a rate sufficient to broaden the EPR lines. No corresponding motionally averaged signal has been observed at higher temperatures, however.

In the absence of a fully resolved ^{29}Si hyperfine structure only a tentative outline of the electronic structure can be given: The three doubly occupied valence orbitals probably consist of the bonding combinations of the dangling-bond orbitals $(b+c)$ (on the two tin atoms), $(d+e)$, and $(a+f)$. The latter combination may be strongly asymmetric owing to the presence of the tin atoms close to (a). The unpaired electron is expected to reside in the likewise asymmetric, antibonding combination of (a) and (f), in agreement with the anisotropy of the g tensor, which corresponds to a spin population in a dangling-bond orbital lying in the $(1\bar{1}0)$ plane.

4. ^{119}Sn hyperfine splittings

The present experiments revealed neither the absolute nor the relative signs of the ^{119}Sn hyperfine parameters except that all three principal hyperfine components for SnV_2^- were shown to have the same sign. In SnV^0 the ^{119}Sn hyperfine parameters are positive,²² thus representing a small negative electron spin density at the tin nucleus, which arises from some kind of spin polarization. This probably also applies to Sn_2V_2^-a : since the tin atoms here lie in the node plane of ψ_u , at least the isotropic part of the hyperfine interaction must stem from spin polarization. Symmetry does not prohibit a dipolar hyperfine interaction with axis perpendicular to the node plane, i.e., along the principal axis X , associated with a direct contribution of the two $5p_X(\text{Sn})$ orbitals to ψ_u . However, if A_X^{Sn} has the same sign as A_Y^{Sn} and A_Z^{Sn} , this contribution is negligible, whereas if A_X^{Sn} has the opposite sign, the dipolar hyperfine interaction will correspond to a spin population of 0.44 e in the $5p_X(\text{Sn})$ orbitals. This seems quite unrealistic since the spin density accounted for by the silicon hyperfine splittings of Sn_2V_2^-a already exceeds the total spin density seen in V_2^- itself and in SnV^0 . Thus we may infer that the principal values of \mathbf{A}^{Sn} for Sn_2V_2^-a all have the same sign, so that the observed hyperfine interaction arises solely from spin polarization. The induced spin population per tin atom of Sn_2V_2^-a is about 60% of that observed in SnV^0 (Table I). In SnV_2^- no symmetry constraints prevent the $5s$ and $5p$ valence orbitals on tin from contributing to ψ_u . Nevertheless, the isotropic hyperfine in-

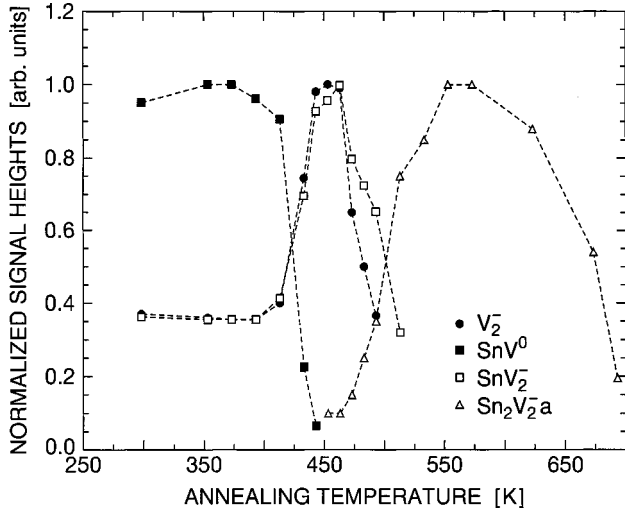


FIG. 11. Changes of the heights of the EPR signals from SnV^0 , SnV_2^- , V_2^- , and Sn_2V_2^-a , resulting from a series of isochronal annealings (30 min) of an n -type sample. The signal heights were measured after cooling the sample to 110 K in ambient light, which ensured reproducible results.

teraction is *smaller* in SnV_2^- than in Sn_2V_2^-a , thus suggesting that a small positive spin density arising from a nonzero amplitude of ψ_u on the tin atom nearly cancels the negative contribution from the spin polarization of the core orbitals. The balance between the two contributions may depend critically on the mean position of the tin nucleus with respect to the silicon atoms carrying the electron spin. Hence, the very unusual temperature dependence of the ^{119}Sn hyperfine parameters for SnV_2^- (Fig. 4) probably arises from anharmonic components of the large-amplitude motion associated with the jumps between pairs of equivalent configurations.

C. Thermal and light-induced processes

Annealings in the temperature range 400–700 K lead to the decay of G29 (SnV^0) and DK4 (SnV^-) signals ($T_a \approx 430$ K) and to a simultaneous growth of the DK1 (SnV_2^-) and G7 (V_2^-) signals. These signals begin to decay at 470 K [$T_a(\text{G7}) \approx 490$ K, $T_a(\text{DK1}) \approx 520$ K], giving way to the signals DK2 (Sn_2V_2^-a) and DK3 (Sn_2V_2^-b), which in turn decay at ≈ 690 K. Figure 11 illustrates these spectral changes as measured after isochronal annealings (30 min at each temperature) and subsequent cooling to 110 K in ambient light. The figure suggests that the decay of SnV^0 is accompanied by the formation of divacancies (SnV_2^- as well as V_2^-) in agreement with the earlier observations by Svensson and Lindström.⁴⁴ Seeking to establish a connection between these processes, we monitored also the decay of G29 and the growth of DK1 and G7 resulting from a series of isothermal annealings at 428 K. After each annealing the sample was cooled to 110 K in the dark and the heights h of these signals and of GGA-2 were measured both before and after illumination for 30 s with band-gap light. The relative rate of decay $-(1/h)(dh/dt)$ for G29, measured before the light flash, was initially $2.2 \times 10^{-4} \text{ s}^{-1}$, decreased to $1.4 \times 10^{-4} \text{ s}^{-1}$ during the first half of the decay, and remained nearly constant thereafter. The height $h(\text{GGA-2})$ increased by a factor

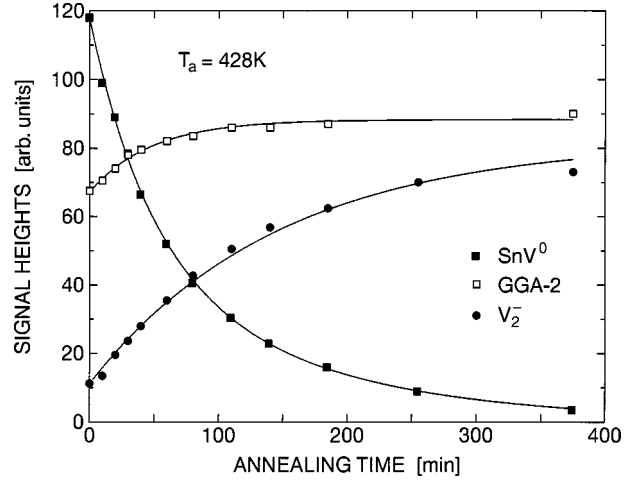


FIG. 12. Decay of the G29 (SnV^0) signal and growth of the G7 (V_2^-) and GGA-2 signals, observed during isothermal annealing of an n -type sample at 428 K. G29 and GGA-2 were measured after cooling the sample to 110 K in the dark, while G7 was measured after a subsequent illumination for 30 s with band-gap light. Continuous curves represent fits to the data obtained with the first-order expressions $h(t) = h_1^0 \exp(-k_1 t) + h_2^0 \exp(-k_2 t)$ (decay of SnV^0) and $h_i(t) = h_i^\infty [1 - \exp(-k_i t)] + h_i^0$ (growth of GGA-2 and V_2^-). The values $k_1 = 3.5 \times 10^{-4} \text{ s}^{-1}$ and $k_2 = 1.2 \times 10^{-4} \text{ s}^{-1}$ describing the decay of SnV^0 were used as fixed parameters ($=k_i$) in the fit to the growth of GGA-2 and V_2^- , respectively.

of 1.34 during the decay of SnV^0 , whereas $h(\text{V}_2^-)$ and $h(\text{SnV}_2^-)$, measured after illumination, increased by factors of 6.5 and 5.3, respectively. As shown in Fig. 12 the decay of SnV^0 may be represented by the expression $h(t) = h_1^0 \exp(-k_1 t) + h_2^0 \exp(-k_2 t)$, with $h_1^0 \approx h_2^0$, $k_1 = 3.5 \times 10^{-4} \text{ s}^{-1}$, and $k_2 = 1.2 \times 10^{-4} \text{ s}^{-1}$. Moreover, the growths of $h(\text{GGA-2})$ and $h(\text{V}_2^-)$ may be fitted with the expression $h_i(t) = h_i^\infty [1 - \exp(-k_i t)] + h_i^0$, where h_∞ and h_i^0 represent signal heights observed at time $t \rightarrow \infty$ and at $t = 0$, respectively, and with k_i equal to k_1 for GGA-2 and k_i equal to k_2 for V_2^- . Figure 13 shows that $h(\text{SnV}_2^-)$ is linearly related to $h(\text{V}_2^-)$ throughout the annealing, indicating that SnV_2^- and V_2^- are formed in a constant proportion. These results strongly suggest that the formation of V_2^- and SnV_2^- is linked to the slow component of the decay of SnV^0 with rate constant k_2 , while other products like GGA-2 result from the fast component described by k_1 .

The decay of SnV^0 occurs here at a temperature that is about 60° lower than the temperature of decay reported by Watkins,²² but which, on the other hand, agrees with the characteristic temperature for the relaxation of stress-induced alignment of SnV^0 (Ref. 22). Indeed, if an attempt frequency $\nu = 10^{13} \text{ s}^{-1}$ is assumed, a fit to the isochronal annealing of the alignment (Fig. 7 of Ref. 22) yields an activation energy of 1.38 eV, leading in turn to the rate constant $k = 5.3 \times 10^{-4} \text{ s}^{-1}$ at 428 K. Hence the reorientation of SnV^0 appears to be only slightly faster than the thermal decay at 428 K, described by the rate constants k_1 and k_2 , in striking contrast to the ratio of $\approx 10^5$ displayed by the rates of the corresponding processes for the E centers, a value taken to indicate that these defects perform about 10^5 reorientations (with associated displacements of the impurity atom) before

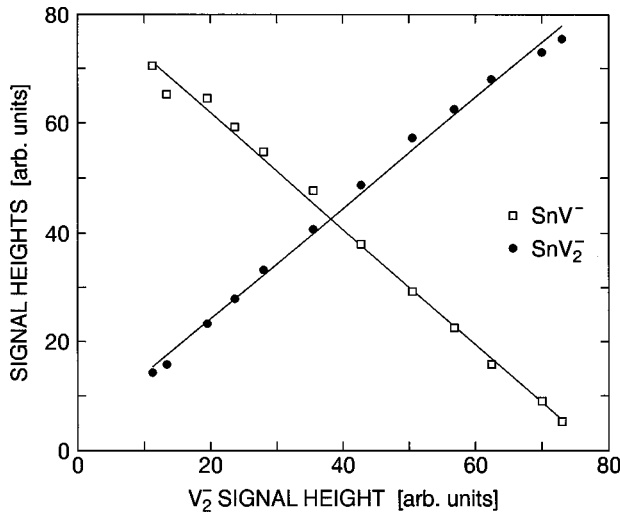
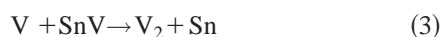


FIG. 13. Relationship between the changes of the signal heights $h(SnV^-)$, $h(SnV_2^-)$, and $h(V_2^-)$, resulting from the isothermal annealing at 428 K. $h(SnV_2^-)$ and $h(V_2^-)$ were measured at 110 K after illumination, whereas $h(SnV^-)$ was taken as the light-induced decrease of $h(SnV^0)$. The linear relationships show that the rate of formation of SnV_2^- and the rate of decay of SnV^- are both proportional to the rate of formation of V_2^- , thus indicating a parallel formation of SnV_2^- and V_2^- , and suggesting that the sum of the amounts of SnV^- , SnV_2^- , and V_2^- is constant.

they become destroyed by encountering other defects. The strongly deviating result for SnV^0 may be explained, however, recalling that the reorientation involves two successive jumps of the vacancy away from the impurity atom. After the second jump the vacancy, now in the third-nearest-neighbor position to the impurity, is still bound electrostatically if the impurity is a group-V atom, whereas the absence of such an attraction to the isoelectronic impurity tin may enable the vacancy to escape from SnV with considerable probability. Hence, the rate of the decay of the stress alignment may, for SnV , characterize the complete dissociation of the defect rather than its vacancy-assisted migration.

The fate of an escaping vacancy will either be to return to the tin atom or to become trapped at another impurity or defect. In the samples examined by Watkins the substitutional tin atoms apparently were the dominant vacancy traps so that no loss of SnV^0 was noticed during a 15-min annealing at 453 K, whereas in the present samples, which have received a ten times higher electron dose and, in addition, contain a substantial amount of carbon, the vacancies escaping from SnV^0 eventually become trapped at defects other than substitutional tin even at 428 K. The parallel formation of V_2^- and SnV_2^- with rate constant k_2 (Fig. 13) suggests the following mechanism



with fixed relative probabilities of the competing processes (2) and (3). The observed kinetics may be interpreted by assuming that SnV^0 initially exists in two almost equally abundant "configurations" A and B ; in A the vacancy trap

(other than Sn) closest to SnV is another SnV , whereas in B the closest vacancy trap is some other defect. At 428 K, the configurations A and B decay independently in first-order processes with somewhat different rate constants, A yielding the products V_2 and SnV_2 according to the processes (1)–(3) and B yielding the defect GGA-2 and probably other products as well.

As noted previously, the EPR signals from V_2^- and SnV_2^- can only be observed after illumination of the sample at low temperature, which in addition converts some SnV^0 into SnV^- . In Fig. 13, we show that the amount of SnV^- , measured as the light-induced decrease of $h(SnV^0)$, is linearly related to the amount of V_2^- and, hence, also to the amount of SnV_2^- , throughout the annealing at 428 K. This suggests that the sum of the amounts of SnV^- , V_2^- , and SnV_2^- , is constant, so that after each step of the annealing the same number of electrons (estimated from the slope of the plot to be approximately half the initial number of SnV^0) are made available by the illumination at 110 K. The light apparently transforms some other defects, including GGA-2, into metastable states having a lower electronic charge than the ground state, thereby providing electrons for distribution among the initially empty ($-/0$) levels of V_2 and SnV_2 , and the sparsely populated ($-/0$) level of SnV .

In the above discussion of the thermal processes, we have tacitly assumed that the fraction of the total amount of divacancies (with or without tin) found in the observable negative charge state after the illumination is independent of the annealing stage, so that the signal heights $h(V_2^-)$ and $h(SnV_2^-)$ faithfully represent *all* divacancies present. This is no trivial assumption, however, and it is not valid for the light-induced conversion of SnV^0 into SnV^- , which increases with the decay of SnV^0 from 40% initially to 65% at the end. Therefore, in the absence of a direct measurement of the amounts of V_2^0 and SnV_2^0 , our interpretation of the observed kinetics must remain tentative, and plausible alternatives may exist. Thus, the data presented in Fig. 13 could be taken to indicate that fixed amounts of V_2^0 and SnV_2^0 , all formed during the electron irradiation, get an increasing share of the electrons made available by the light as SnV^0 decays. Hence, the present results suggest, but do not prove, that the thermal decay of SnV^0 at 428 K is accompanied by formation of divacancies. However, irrespective of the interpretation, the slope of the plot of $h(SnV^-)$ vs $h(V_2^-)$ in Fig. 13 strongly suggests that the sum of the amounts of V_2^- and SnV_2^- after the decay of SnV^0 is roughly half the initial amount of SnV^0 . With the introduction rate estimated above for SnV^0 (0.03 cm^{-1}) this in turn suggests that the overall efficiency of the formation of divacancies in our tin-doped samples, as measured after the decay of SnV^0 , equals that reported by Watkins and Corbett for Czochralski material that was electron-irradiated under similar conditions.¹¹

The decay of V_2^- and SnV_2^- and the simultaneous formation of $Sn_2V_2^-$ (see Fig. 11) were monitored during a series of annealings at 503 K. The observed spectral changes, measured after illumination at 110 K as before, are shown in Fig. 14. The signals from V_2^- and SnV_2^- both decay in first-order processes with rate constants $k_3 = 3.5 \times 10^{-4} \text{ s}^{-1}$ and $k_4 = 1.8 \times 10^{-4} \text{ s}^{-1}$, respectively, while the signal from

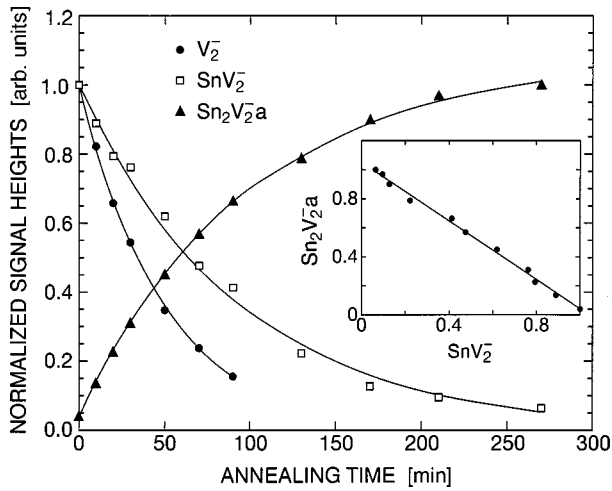
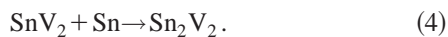


FIG. 14. Decay of the G7 (V_2^-) and DK1 (SnV_2^-) signals and growth of the DK2 ($\text{Sn}_2V_2^-a$) signal resulting from isothermal annealing at 503 K. The signal heights were measured at 110 K after illuminating the sample with band-gap light. First-order fits to the decays (continuous curves) yield the rate constants $k_3=3.5 \times 10^{-4} \text{ s}^{-1}$ and $k_4=1.8 \times 10^{-4} \text{ s}^{-1}$ for V_2^- and SnV_2^- , respectively. The growth of $\text{Sn}_2V_2^-a$ is calculated from $h(t)=[1-\exp(-k_4t)]+h^0$, with $k_4=1.8 \times 10^{-4} \text{ s}^{-1}$. The inset shows a linear relationship between the signal heights of SnV_2^- and $\text{Sn}_2V_2^-$, confirming that the rate of formation of $\text{Sn}_2V_2^-a$ is proportional to the rate of decay of SnV_2^- throughout the annealing.

$\text{Sn}_2V_2^-a$ grows in. The inset shows the observed linear relationship between $h(\text{SnV}_2^-)$ and $h(\text{Sn}_2V_2^-)$, indicating that the rate of formation of $\text{Sn}_2V_2^-a$ is proportional to the rate of decay of SnV_2^- [the height of the signal from $\text{Sn}_2V_2^-b$, not measured in this experiment, was observed in the isochronal annealing to change strictly in proportion to $h(\text{Sn}_2V_2^-a)$]. To confirm the relationship between SnV_2^- and $\text{Sn}_2V_2^-$, we show in Fig. 14 that the measured growth of $\text{Sn}_2V_2^-a$ is accurately reproduced by the first-order expression $h(t)=h^\infty[1-\exp(-k_4t)]+h^0$ with the value of k_4 derived from the decay of SnV_2^- . The sum of the intensities of the signals from $\text{Sn}_2V_2^-a$ and $\text{Sn}_2V_2^-b$ estimated at the end of the annealing is about 60% of the intensity of the signal from SnV_2^- before the annealing.

Taking the signal heights $h(\text{SnV}_2^-)$ and $h(\text{Sn}_2V_2^-a)$, measured after the light flash to represent the total amounts of SnV_2 and Sn_2V_2 , respectively, we may interpret the observed linear relationship between the heights in terms of the reaction



The somewhat faster decay of V_2 apparently occurs in an unrelated process. The divacancy is known to reorient rapidly at 500 K, which implies that it also moves in the lattice.¹⁰ The mechanism is shown schematically in Fig. 15(a). As with SnV^0 , the temperature of decay observed here for V_2 is substantially lower than that reported by Watkins,¹⁰ thus pointing to a higher concentration of traps also for V_2 in our samples. Tin, the dominant impurity, might be assumed to trap V_2 , forming SnV_2 . However, this process cannot account for the decay of V_2 , since no change in the rate of

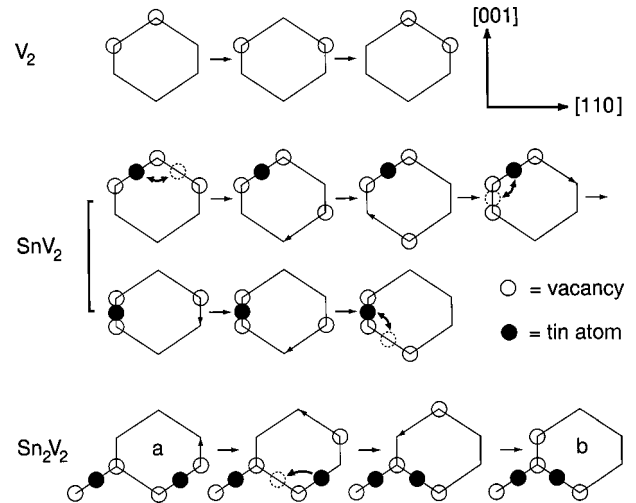


FIG. 15. Schematic representation of the migration of V_2 (top), the proposed mechanism for migration of SnV_2 (middle), and the application of this mechanism to Sn_2V_2 (bottom), projected on the $(1\bar{1}0)$ plane of the silicon lattice. Curved double arrows in SnV_2 connect the two equivalent positions of the tin atom. In Sn_2V_2 the mechanism transforms one form of the defect [(a) or (b)] into the other without moving the defect with respect to the lattice.

decay of SnV_2^- is observed at the stage when V_2^- has practically disappeared (see Fig. 14).

The occurrence of the reaction (4) indicates that SnV_2 , like V_2 itself, moves in the lattice at 500 K. Apparently, the V_2 moiety of the complex drags the tin atom a moderate distance ($\approx 10 \text{ nm}$) through the lattice until it encounters a second tin atom and forms Sn_2V_2 . A plausible mechanism for the movement of SnV_2 is represented schematically in Fig. 15(b): The conventional vacancy-assisted diffusion of impurities is here modified to incorporate the fact that the tin atom in SnV_2 has two equivalent positions within the “trivacancy,” between which it probably jumps freely at 500 K. Recalling that the migrating V_2 has no affinity to substitutional tin atoms, it may seem surprising that all SnV_2 do not permanently disintegrate as a consequence of the dissociation into $\text{SnV} + \text{V}$, since SnV is unstable at 500 K. However, owing to the unique structure of SnV , the jumping vacancy is never removed further from another vacancy than to the second-nearest-neighbor position, implying that a substantial binding energy (of the order of 0.6 eV, Ref. 10) is retained. Moreover, the initial dissociation of the divacancy of SnV_2 is the rate-determining step, having an energy of activation $E_a \approx 1.3 \text{ eV}$, whereas the subsequent steps, which correspond to diffusion of a monovacancy ($E_a \approx 0.3 \text{ eV}$) may be ten orders of magnitude faster. Hence, the vacancy of SnV has little opportunity to leave the tin atom ($E_a \approx 1-1.4 \text{ eV}$) while the other vacancy is on its way around the hexagon.

Application of the proposed diffusion mechanism to Sn_2V_2 merely leads to a reversible transformation of one form into the other, as illustrated in Fig. 15(c). This accounts for the observation that $\text{Sn}_2V_2^-a$ and $\text{Sn}_2V_2^-b$ are kinetically indistinguishable, and also for the high-annealing temperature (690 K) as compared to that of V_2 and SnV_2 , which both disappear because they become mobile in the lattice at 500 K.

IV. SUMMARY AND CONCLUSIONS

Our main experimental findings may be summarized as follows: Irradiation with 2 MeV electrons at room temperature of *n*-type float-zone silicon doped with 10^{18} cm^{-3} tin generates the tin-vacancy complex SnV. After cooling the sample in the dark, SnV is observed by EPR mainly as SnV^0 ; however, below 15 K a weak signal from SnV^- is also observed,⁴¹ which increases strongly at the expenses of SnV^0 by illumination with light. Light also makes rather weak signals from $(\text{V}-\text{V})^-$ and $(\text{SnV}-\text{V})^-$ appear.

Annealing at 428 K removes the signals from SnV^0 and SnV^- and increases those from $(\text{V}-\text{V})^-$ and $(\text{SnV}-\text{V})^-$ by a factor of 5-6. The kinetics indicates that about 50% of the decaying SnV end up as $(\text{V}-\text{V})^-$ or $(\text{SnV}-\text{V})^-$ in this process, which probably involves dissociation of SnV and the subsequent reaction of the escaping vacancies with still undissociated SnV. No evidence for (mono) vacancy-assisted migration of tin was obtained. Further annealing at 503 K removes $(\text{V}-\text{V})^-$ and $(\text{SnV}-\text{V})^-$, converting a large fraction of the latter into either $(\text{SnV}-\text{VSn})^-$ or $(\text{Sn}_2\text{V}-\text{V})^-$, which in turn disappear by annealing of the sample at 690 K. Thus, the presence of tin is found to delay the thermal formation of divacancies by forming the intermediate SnV, in agreement with observations made by other techniques; but in contrast to these earlier results, we find that a substantial fraction of the divacancies arising from the decay of SnV are bound to tin atoms, which endows them with an unexpected thermal stability. The modifications of the basic structure and properties of the divacancy brought about by substituting tin for one or two silicon atoms adjacent to the divacancy include a lowering of the symmetry of $(\text{SnV}-\text{V})^-$ from C_{1h} to C_1 , a change of the symmetry of the ground state of $(\text{SnV}-\text{VSn})^-$ from B_u to A_u and, generally, a redistribution of electron spin density among the silicon atoms bordering the divacancy. However, no significant spin density is found on the tin atoms, and the

singly occupied orbital remains an anti-bonding combination of dangling-bond orbitals on silicon atoms, indicating that the electrical properties of the isolated divacancy are essentially retained. The observed modifications may be ascribed mainly to an obvious difference between tin and silicon: the larger size of the tin atom. This causes tin to move from the substitutional position towards the center of the adjacent vacancy and, moreover, enables it to interact electronically with silicon atoms nominally in second-nearest-neighbor positions, as demonstrated earlier for SnV^0 . Moreover, the substantially lower first ionization potential of the tin atom compared to that of silicon appears to affect significantly the bonding and the spin distribution within the defects.

Although the EPR signals do not reveal the precise location of the tin atoms, we may in analogy with the structure of SnV^0 represent $(\text{SnV}-\text{V})^-$ as a trivacancy with a tin atom located near one of the two equivalent "bond-center" positions, and $(\text{SnV}-\text{VSn})^-$ and $(\text{Sn}_2\text{V}-\text{V})^-$ as planar and pyramidal tetravacancies, respectively, each with two tin atoms near pairs of equivalent bond-center positions. This representation of $(\text{SnV}-\text{V})^-$, suggesting a low barrier between two equivalent position of the tin atom, serves to explain how $(\text{SnV}-\text{V})^-$ migrates in the lattice at 500 K, as required by the observed transformation into $(\text{SnV}-\text{VSn})^-$ and $(\text{Sn}_2\text{V}-\text{V})^-$, whereas the tetravacancy model of these defects accounts for their stability and identical kinetics of formation and decay.

ACKNOWLEDGMENTS

The tin-doped samples used in this investigation were kindly supplied by J. L. Lindström, Dept. of Solid State Physics, University of Lund, and their tin content was determined by B.G. Svensson, Dept. of Solid State Electronics, KTH, Kista-Stockholm. Many stimulating and fruitful discussions with B. Bech Nielsen and A. Nylandsted Larsen are gratefully acknowledged.

*Present address: Laboratorio MDM-INFM, Via C. Olivetti 2, I-20041 Agrate Brianza (MI), Italy.

¹G.D. Watkins, J. Phys. Soc. Jpn. Suppl. II **18**, 22 (1963).

²G.D. Watkins, in *Radiation Damage in Semiconductors*, edited by P. Baruch (Dunod, Paris, 1965), p. 97.

³G.D. Watkins, in *Radiation Damage and Defects in Semiconductors 1972*, edited by J. E. Whitehouse (Institute of Physics, London, 1973), p. 228.

⁴G.D. Watkins, in *Lattice Defects in Semiconductors 1974*, edited by F.A. Huntley (Institute of Physics, London, 1975), p. 1.

⁵G.D. Watkins and J.R. Troxell, Phys. Rev. Lett. **44**, 593 (1980).

⁶G.D. Watkins, A.P. Chatterjee, and R.D. Harris, in *Defects and Radiation Effects in Semiconductors 1980*, edited by R. Hasiguti (Institute of Physics, London, 1981), p. 199.

⁷J.L. Newton, A.P. Chatterjee, R.D. Harris, and G. Watkins, Physica B **116**, 219 (1983).

⁸M. Sprenger, S.H. Muller, E.G. Sieverts, and C.A.J. Ammerlaan, Phys. Rev. B **35**, 1566 (1987).

⁹J.W. Corbett and G.D. Watkins, Phys. Rev. Lett. **7**, 314 (1961).

¹⁰G.D. Watkins and J.W. Corbett, Phys. Rev. **138**, A543 (1965).

¹¹J.W. Corbett and G.D. Watkins, Phys. Rev. **138**, A555 (1965).

¹²C.A.J. Ammerlaan and G.D. Watkins, Phys. Rev. B **5**, 3988 (1972).

¹³J.G. de Wit, E.G. Sieverts, and C.A.J. Ammerlaan, Phys. Rev. B **14**, 3494 (1976).

¹⁴E.G. Sieverts, S.H. Muller, and C.A.J. Ammerlaan, Phys. Rev. B **18**, 6834 (1978).

¹⁵E.G. Sieverts, M. Sprenger, and C.A.J. Ammerlaan, Phys. Rev. B **41**, 8630 (1990).

¹⁶G.D. Watkins and J.W. Corbett, Phys. Rev. **134**, A1359 (1964).

¹⁷E.L. Elkin and G.D. Watkins, Phys. Rev. **174**, 881 (1968).

¹⁸G.D. Watkins, Phys. Rev. B **13**, 2511 (1976).

¹⁹M. Sprenger, R. Van Kamp, E.G. Sieverts, and C.A.J. Ammerlaan, J. Electron. Mater. **14a**, 815 (1985).

²⁰G.D. Watkins, Phys. Rev. **155**, 802 (1967).

²¹G.D. Watkins, IEEE Trans. Nucl. Sci. **NS-16**, 13 (1969).

²²G.D. Watkins, Phys. Rev. B **12**, 4383 (1975).

²³G.D. Watkins, Solid State Commun. **17**, 1205 (1975).

²⁴G.D. Watkins and J.W. Corbett, Phys. Rev. **121**, 1001 (1961).

²⁵J.W. Corbett, G.D. Watkins, R.M. Chrenko, and R.S. McDonald, Phys. Rev. **121**, 1015 (1961).

²⁶K.L. Brower, Phys. Rev. B **4**, 1968 (1971).

²⁷H.H. Woodbury and G.W. Ludwig, Phys. Rev. Lett. **5**, 96 (1960).

²⁸S.H. Muller, G.M. Tuynman, E.G. Sieverts, and C.A.J. Ammerlaan, Phys. Rev. B **25**, 25 (1982).

²⁹A. Brelot, IEEE Trans. Nucl. Sci. **NS-19**, 220 (1972).

- ³⁰A. Brelet, in *Radiation Damage and Defects in Semiconductors*, edited by J.E. Whitehouse, Conference Series No. 16 (Institute of Physics, London and Bristol, 1973), p. 191.
- ³¹B.G. Svensson, J. Svensson, J.L. Lindström, D. Davies, and J.W. Corbett, *Appl. Phys. Lett.* **51**, 2257 (1987).
- ³²K.L. Brower, *Radiat. Eff.* **8**, 213 (1971).
- ³³P. Stallinga, P. Johannesen, S. Herstrom, K. Bonde Nielsen, B. Bech Nielsen, and J.R. Byberg, *Phys. Rev. B* **58**, 3842 (1998).
- ³⁴D.F. Daly and K.A. Pickar, *Appl. Phys. Lett.* **15**, 267 (1969).
- ³⁵A.V. Dvurechenskii and A.A. Karanovich, *Fiz. Tekh. Poloprovodn* **19**, 1944 (1985) [*Sov. Phys. Semicond.* **19**, 1198 (1985)].
- ³⁶L.C. Allen, H.M. Gladney, and S.H. Glarum, *J. Chem. Phys.* **40**, 3135 (1964).
- ³⁷S.H. Glarum, *Rev. Sci. Instrum.* **36**, 771 (1965).
- ³⁸N. Bjerre, *J. Chem. Phys.* **76**, 3347 (1982).
- ³⁹H. Horiye and E.G. Wikner, *J. Appl. Phys.* **40**, 3879 (1969).
- ⁴⁰J.R. Byberg, B. Bech Nielsen, M. Fanciulli, S.K. Estreicher, and P.A. Fedders (unpublished).
- ⁴¹M. Fanciulli and J.R. Byberg, *Physica B* (to be published).
- ⁴²H. Goldstein, *Classical Mechanics* (Addison-Wesley, Reading, MA, 1950), p. 109.
- ⁴³*Handbook of Physics*, edited by E.U. Condon and H. Odishaw (McGraw-Hill, New York, 1958).
- ⁴⁴B.G. Svensson and J.L. Lindström, *J. Appl. Phys.* **72**, 5616 (1992).